



Cross-linked polyelectrolyte reinforced SnO₂ electron transport layer for robust flexible perovskite solar cells

Zhihao Li^{a,b,c,d}, Zhi Wan^a, Chunmei Jia^a, Meng Zhang^{a,b,c}, Meihe Zhang^{b,c}, Jiayi Xue^a, Jianghua Shen^{b,c}, Can Li^{a,d}, Chao Zhang^{b,c,*}, Zhen Li^{a,d,*}

^a State Key Laboratory of Solidification Processing, Center for Nano Energy Materials, School of Materials Science and Engineering, Northwestern Polytechnical University and Shaanxi Joint Laboratory of Graphene (NPU), Xi'an 710072, Shaanxi, China

^b Department of Aeronautical Structure Engineering, School of Aeronautics, Northwestern Polytechnical University, Xi'an 710072, Shaanxi, China

^c Shaanxi Key Laboratory of Impact Dynamics and Its Engineering Application, Joint International Research Laboratory of Impact Dynamics and Its Engineering Applications, Xi'an 710072, Shaanxi, China

^d Research & Development Institute of Northwestern Polytechnical University in Shenzhen, Shenzhen 519057, Guangdong, China

ARTICLE INFO

Article history:

Received 6 April 2023

Revised 12 May 2023

Accepted 21 June 2023

Available online 4 July 2023

Keywords:

Polyelectrolyte

Cross-link

Tin oxide

Electron transfer layer

Flexible solar cells

ABSTRACT

SnO₂ electron transport layer (ETL) is a vital component in perovskite solar cells (PSCs), due to its excellent photoelectric properties and facile fabrication process. In this study, we synthesized a water-soluble and adhesive polyelectrolyte with ethanolamine (EA) and poly-acrylic acid (PAA). The linear PAA was crosslinked by EA, forming a 3D network that stabilized the SnO₂ nanoparticle dispersion. An organic-inorganic hybrid ETL is developed by introducing the cross-linked PAA-EA into SnO₂ ETL, which prevents nano particle agglomeration and facilitates uniform SnO₂ film formation with fewer defects. Additionally, the PAA-EA-modified SnO₂ facilitated a uniform and compact perovskite film, enhancing the interface contact and carrier transport. Consequently, the PAA-EA-modified PSCs exhibited excellent PCE of 24.34% and 22.88% with high reproducibility for areas of 0.045 and 1.00 cm², respectively. Notably, owing to structure reinforce effect of PAA-EA in SnO₂ ETL, flexible device demonstrated an impressive PCE of 23.34% while maintaining 90.1% of the initial PCE after 10,000 bending cycles with a bending radius of 5 mm. This successful approach of polyelectrolyte reinforced hybrid organic-inorganic ETL displays great potential for flexible, large-area PSCs application.

© 2023 Science Press and Dalian Institute of Chemical Physics, Chinese Academy of Sciences. Published by ELSEVIER B.V. and Science Press. All rights reserved.

1. Introduction

Perovskite solar cells (PSCs) have garnered significant research interest due to its excellent optoelectronic characteristic [1–5], resulting in the power conversion efficiency (PCE) increased sharply from 3.8% to 25.7% over the past decade, approaching that of commercial silicon cells [6–10]. However, the charge transport layers, critical for extracting and separating carriers, are equally important in achieving high-performance solar cells [11]. As the widely used electron transport layer (ETL), titanium dioxide (TiO₂) requires high temperature sintering processes (>450 °C), making it unsuitable for fabricating flexible devices [12–17]. Furthermore, the intrinsic high photocatalytic nature of TiO₂ leads to

poor light long-term stability of PSCs [18,19]. SnO₂ is an excellent candidate ETL material for PSCs, with higher conductivity, lower processing temperature and lower photooxidation reactivity [20–25]. However, the SnO₂ nanoparticles are usually stored in colloidal solution, which is unstable and tends to form aggregation over time [26–28]. The particle aggregation causes pinholes and non-uniformity in SnO₂ ETL over large area, which limits its use in large-area solar modules [29–36]. Additionally, inorganic SnO₂ films are stiff and mechanically brittle, making them prone to crack and delaminate in flexible PSCs (f-PSCs) under repeated bending fatigue [37–45].

To address the challenges associated with SnO₂ as a crucial ETL layer in flexible PSCs, a combination of organic substances and inorganic ETL is a promising approach to enhance physical and electrical contact between SnO₂ nanoparticles and achieves a robust and uniform ETL [46–49]. Introducing functional molecules such as heparin potassium (HP) into SnO₂ colloids has been shown

* Corresponding authors.

E-mail addresses: chaozhang@nwpu.edu.cn (C. Zhang), lizhen@nwpu.edu.cn (Z. Li).

to realize a dense and uniform SnO_2 layer, and the enhanced wettability profits to achieve a good coverage of the perovskite film on the ETL [50]. The HP can act as a glue between SnO_2 nanoparticles to increase the tenacity of the films. These improvements lead to a durable f-PSC with 93% efficiency retaining after 500 bending cycles. Polyethylene glycol was also introduced into SnO_2 colloid to mitigate issues such as pinholes and agglomeration, resulting in improved device performance [51]. The use of polyacrylic acid (PAA) to stabilize tin (IV) SnO_2 colloid has been demonstrated to reduce surface defects and suppress nonradiative recombination, realizing a high operational stability and a certified PCE of 25.4%. A perovskite module was fabricated using PAA- SnO_2 with a PCE of 20.56%, demonstrating its potential in large-area application [10]. These approaches demonstrate the potential for combining advantages of organic and inorganic compounds to produce hybrid ETLs that can improve the functional properties and toughness of individual layers in PSCs. Therefore, the incorporation of polymers reinforcements into SnO_2 colloids to construct organic-inorganic hybrid ETLs is a powerful strategy to improve efficiency and stability of PSCs [52,53].

Herein, we synthesized a water-soluble and adhesive polyelectrolyte binder (PAA-EA) and added it to SnO_2 nanoparticles to prepare a hybrid organic-inorganic ETL for high-performance PSCs. PAA-EA formed a 3D cross-linking network with SnO_2 , reducing agglomeration and stabilizing nanoparticles. Addition of PAA-EA into SnO_2 also mitigated pinhole formation, presenting a uniform morphology and high-quality perovskite film. The PAA-EA-modified device achieved a high PCE of 24.34%, with 22.88% efficiency for areas of 1 cm^2 , indicating potential for large-area application. The PAA-EA cross-linked SnO_2 nanoparticles enhance the interfacial and mechanical properties, obtaining a high PCE of 23.34% in f-PSC, maintaining 90.1% of initial PCE after 10,000 bending cycles.

2. Results and discussion

The synthesis of PAA-EA involved a straightforward acid-base neutralization reaction and details of which were presented in the experimental section and illustrated in Fig. S1. The molecular structure was confirmed via Fourier transform infrared (FTIR) spectroscopy (Fig. S2). Upon deprotonation of PAA by EA, the linear polymer chains were converted into a robust 3D cross-linked network through electrostatic interactions and hydrogen bonding among the $-\text{COO}^-$, $-\text{NH}_3^+$, and $-\text{OH}$ functional groups [54,55]. The electrostatic repulsion of neighboring $-\text{COO}^-$ groups in PAA-EA weaken the self-associated hydrogen bonds ($-\text{COOH} \cdots \text{HOOC}-$) in PAA, reducing self-agglomeration of the polymer chain and enhancing inter-chain interaction. Moreover, the ionic bonds between $-\text{COO}^-$ and $-\text{NH}_3^+$ in PAA-EA form 3D cross-linking networks, further enhancing the polymer strength (Fig. S3) [56].

As illustrated in Fig. 1(b), the polyelectrolyte can cross-link the SnO_2 colloid to enhance mechanical properties. The resulting PAA-EA- SnO_2 composite possessed a unique organic-inorganic hybrid structure, with the soft organic portion consisting of PAA-EA via hydrogen bonding and electrostatic interactions, and the rigid inorganic segment composed of SnO_2 nanoparticles. The chemical reactions between the soft organic portion and inorganic SnO_2 resulted in a robust hybrid structure with excellent mechanical properties. The tensile strength-strain of SnO_2 and PAA-EA- SnO_2 films on PET flexible substrates were obtained and presented in Fig. 1(c). Notably, the PAA-EA- SnO_2 film exhibited higher tensile strength than the bare SnO_2 film. The enhancement in mechanical properties can be attributed to the presence of the PAA-EA organic component, which contains numerous polar groups that act as anchors to induce mechanical interlocking and establish chemical

bonds with SnO_2 . Moreover, the organic portion of the PAA-EA- SnO_2 composites acted as a buffer zone, with the soft organic network absorbing stress and transferring it to the rigid inorganic nanoparticles, contributing to enhanced energy dissipation during deformation. This unique organic-inorganic hybrid structure effectively reduced stress concentration and promoted stress transmission, resulting in improved mechanical properties.

FTIR measurement was conducted to further investigate the interaction between PAA-EA and SnO_2 (Fig. 1d). There was a shift in the absorption peaks of O-Sn-O stretching bands at 688 cm^{-1} to 678 cm^{-1} upon PAA-EA modification. Additionally, the peak of COO^- stretching vibration in PAA-EA was observed in PAA-EA- SnO_2 and shifted from 1532 cm^{-1} to a higher wavenumber of 1545 cm^{-1} , indicating that PAA-EA can chemically anchor to the SnO_2 surface.

As nanoparticles have a tendency to aggregate due to van der Waals force, we evaluated the effect of PAA-EA on the stability of SnO_2 colloidal solution by measuring the Zeta potential (Fig. 1e and Fig. S4). It was found that the zeta potential of pristine diluted SnO_2 solution decreased from -35.4 to -20.5 mV after 72 h of storage at ambient atmosphere ($20\text{--}25^\circ\text{C}$), resulting in solution changing from transparent to cloudy and opaque (Fig. S5). This indicates that the attraction between particles exceeded the repulsive force, leading to agglomeration and the destruction of dispersion. In contrast, The PAA-EA- SnO_2 showed a higher Zeta potential of -45.1 mV and maintained excellent stability after aging. No visible change was observed in the aged PAA-EA- SnO_2 solution. Furthermore, we measured the particle size of SnO_2 particles using dynamic light scattering (DLS) spectra. The size of pristine SnO_2 increased from 3.26 to 11.41 nm after aging for 72 h. While PAA-EA- SnO_2 exhibited homogeneous dispersion with an average diameter of 4.46 nm before and after aging (Fig. 1f and Fig. S6). The O atoms of $-\text{COO}^-$ and $-\text{OH}$ groups in PAA-EA can bind with Sn atoms in SnO_2 to stabilize the SnO_2 nanoparticles in solution and prevent their agglomeration. We also measured the light transmission of different ETL films in Fig. S7 and found that PAA-EA- SnO_2 showed slightly increased transmission, which may be due to the fact that PAA-EA can reduce light scattering caused by large particle agglomeration in pristine SnO_2 films.

Atomic force microscopy (AFM) measurement was used to characterize the morphology of SnO_2 and PAA-EA- SnO_2 films. The root mean square (RMS) is a parameter that measures the roughness of surface. The RMS value of the SnO_2 film decreased from 1.84 to 1.21 upon PAA-EA modification as shown in Fig. 1(g), indicating that PAA-EA can act as a glue to improve the compactness and smoothness of the ETL. PAA-EA reduced the number of pinholes and achieve better coverage of ETL films, thus reducing leakage current as confirmed by C-V measurements (Fig. S8). The RMS value increased to 4.97 with aged SnO_2 , while the aged PAA-EA- SnO_2 barely changed due to the suppression of particle aggregation, which was consistent with the DLS and zeta potential results. Overall, the AFM results suggest that PAA-EA can enhance the morphology of the SnO_2 ETL, which may lead to improved device performance.

We fabricated a planar PSC with an architecture of ITO/ SnO_2 /perovskite/spiro-OMeTAD/Au to illustrate the effect of PAA-EA on photovoltaic performance (Fig. 2a). The PCE increased with the introduction of PAA-EA, and optimal J-V curves and photovoltaic parameters of PSCs with different PAA-EA concentration were summarized in Fig. S9. The champion PCE with PAA-EA- SnO_2 was 24.34%, with an open circuit voltage (V_{oc}) of 1.171 V , short-circuit current density (J_{sc}) of 25.50 mA cm^{-2} , and fill factor (FF) of 81.48%. Meanwhile, the control device showed a PCE of 22.49% ($V_{\text{oc}} = 1.145\text{ V}$, $J_{\text{sc}} = 25.31\text{ mA cm}^{-2}$ and $FF = 77.59\%$) (Fig. 2b). The PCE distributions of 12 cells (Fig. 2c) showed the improved PCE and high reproducibility of the PAA-EA modifica-

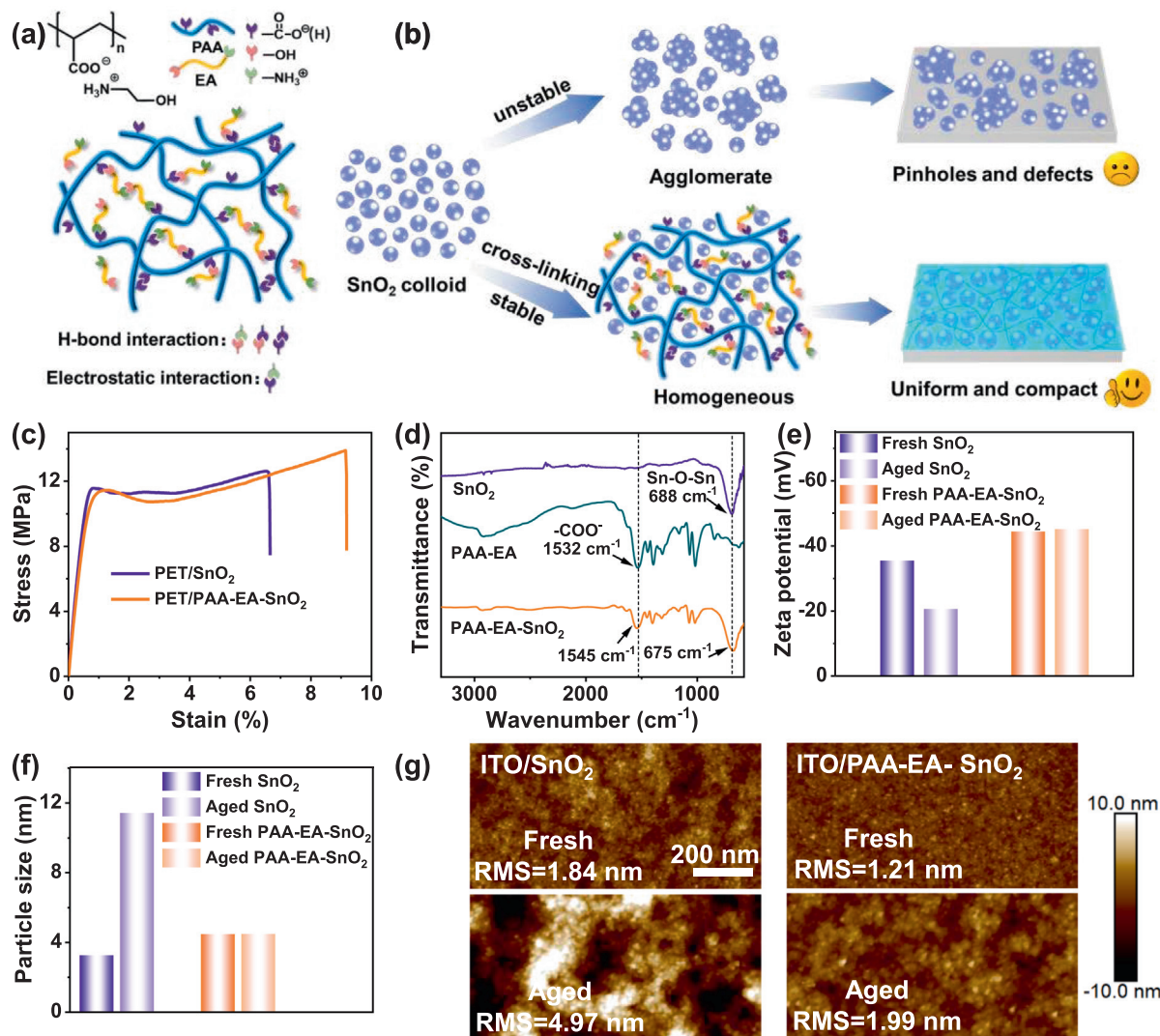


Fig. 1. PAA-EA modification to the SnO₂ colloid and ETLs. (a) Schematic of the PAA-EA structure. (b) Schematic of SnO₂ nanoparticle dispersion with and without PAA-EA. (c) Stress-strain curve of PET/SnO₂ and PET/PAA-EA-SnO₂. (d) FTIR spectra of SnO₂ and PAA-EA-SnO₂ films. (e) Zeta potential of fresh and aged SnO₂ and PAA-EA-SnO₂ colloidal dispersions. (f) Particle size distribution of fresh and aged SnO₂ and PAA-EA-SnO₂ colloidal dispersions. (g) AFM image of fresh and aged SnO₂ and PAA-EA-SnO₂ colloid deposited on ITO substrates.

tion, leading to the average PCE increase from 21.55% to 23.98%. Fig. 2(d) showed the steady-state power outputs (SPO) of devices recorded at maximum-power-point (MPP) voltages. The PAA-EA modified device demonstrated a stabilized PCE of 24.15% over 600 s, which confirmed the improved performance and enhanced stability of PAA-EA modified PSCs under working conditions. Fig. 2(e) showed the incident photo-to-current efficiency (IPCE) spectra to confirm the J_{SC} improvement of PSCs with SnO₂ and PAA-EA-SnO₂ ETLs. The increased IPCE of PAA-EA-SnO₂ device between 350–400 nm could be due to reduced charge recombination at the ETL/perovskite interface, and IPCE improvement between 700–800 nm could be attributed to better built-in potential and fewer shunting paths in the PAA-EA-SnO₂ devices. The integrated J_{SC} obtained from pristine and PAA-EA modified PSCs were 24.42 and 25.27 mA cm⁻², respectively, which were well-matched with the measured J_{SC} from J - V curve. Moreover, we evaluated uniformity of PAA-EA-SnO₂ ETL on ITO substrate when scaling-up to large-area devices, and achieved a competitive PCE of 22.88% in a large-area device (1.00 cm²) with good reproducibility (Fig. 2f and Fig. S11).

X-ray photoelectron spectroscopy (XPS) measurements were used to explore surface characteristics of the SnO₂ ETLs. The appearance of N 1s characteristic peak at 399 eV confirmed the presence of PAA-EA in PAA-EA-SnO₂ (Fig. S12a). The peak positions of Sn 3d of SnO₂ were found to shift to lower binding energy after PAA-EA modification, due to the increasement of electron cloud density around Sn (Fig. 3a). Analysis of O 1s spectra in Fig. S12(b) indicated that peaks at 531.6 and 530.3 eV were related to hydroxyl group (—OH) and lattice oxygen (O²⁻), respectively. After PAA-EA modification, the ratio of —OH/O²⁻ in SnO₂ decreased, which implied that PAA-EA can passivate surface defect and thereby suppress carrier recombination.

We further investigated electrical properties of SnO₂ and PAA-EA-SnO₂ films. The conductivity of SnO₂ and PAA-EA-SnO₂ ETLs was calculated using the following formula

$$\delta = \frac{Id}{VA} \quad (1)$$

where A is effective area (0.045 cm²), d is thickness (30 nm) of ETLs. As shown in Fig. 3(b), the conductivity increased from 1.07×10^{-5} S

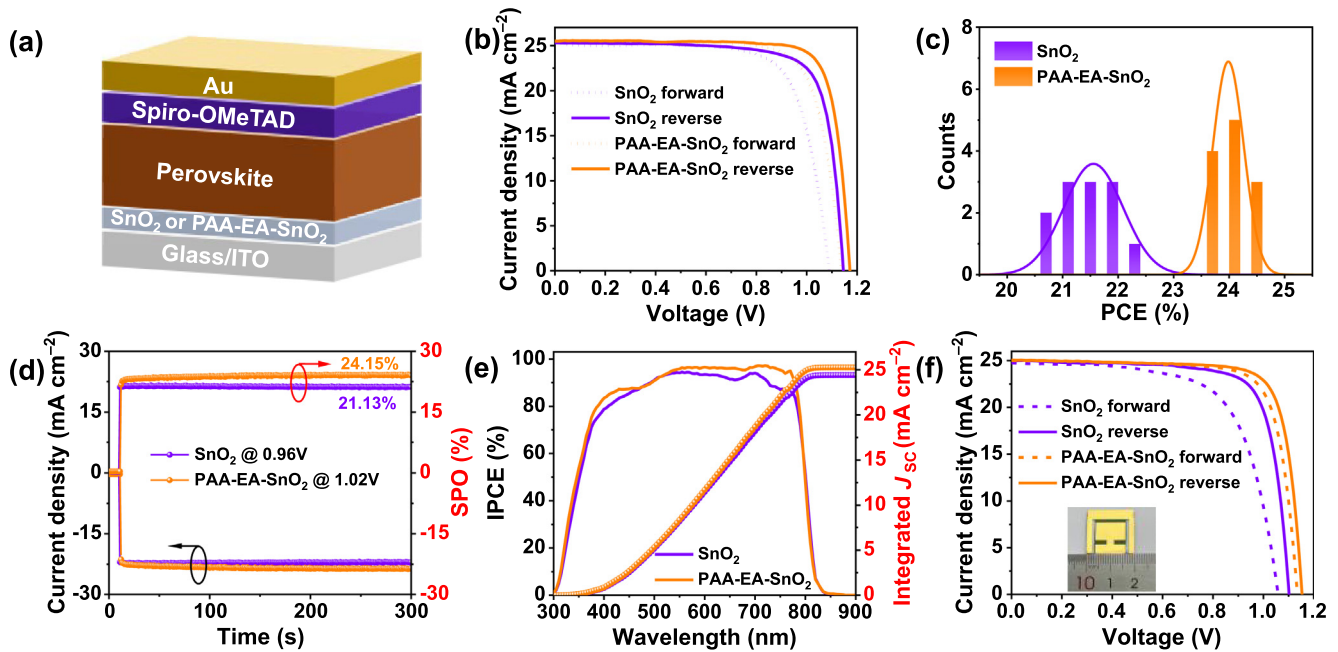


Fig. 2. Perovskite solar cell performance with SnO_2 and PAA-EA- SnO_2 . (a) Device structure of PAA-EA modified perovskite solar cells. (b) J-V curves of best SnO_2 and PAA-EA- SnO_2 devices. (c) The PCE distribution statistics of PSCs with SnO_2 and PAA-EA- SnO_2 . (d) Steady-state current density and SPO of PSCs with SnO_2 and PAA-EA- SnO_2 . (e) IPCE spectra of PSCs with SnO_2 and PAA-EA- SnO_2 . (f) J-V curve of best PAA-EA- SnO_2 PSCs with area of 1 cm^2 .

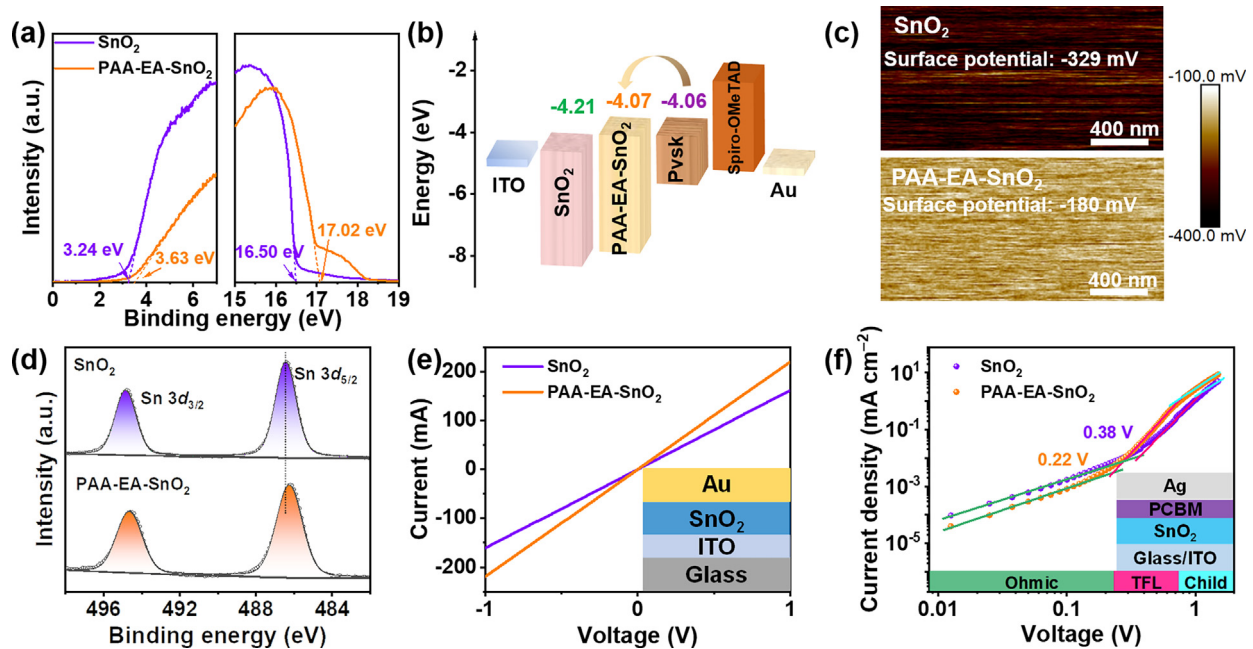


Fig. 3. Optoelectronic characteristics of SnO_2 ETLs. (a) XPS spectra of SnO_2 and PAA-EA- SnO_2 films. (b) Conductivity measurement of SnO_2 and PAA-EA- SnO_2 films. (c) Dark J-V characterization of SnO_2 and PAA-EA- SnO_2 films. (d) UPS spectra of SnO_2 and PAA-EA- SnO_2 ETLs. (e) Energy band diagrams of SnO_2 and PAA-EA- SnO_2 ETLs. (f) KPFM measurement on SnO_2 and PAA-EA- SnO_2 ETLs.

cm^{-1} for SnO_2 to $1.45 \times 10^{-5} \text{ S cm}^{-1}$ for PAA-EA- SnO_2 , which could own to electron doping effect of NH_3^+ groups in PAA-EA [49]. To further investigate the electrical properties of ETLs, electron trap-state density and carrier mobility were obtained using space-charge-limited current (SCLC) measurement (Fig. 3c). The trap density n_t was determined using the formula

$$V_{\text{TFL}} = \frac{qn_t L^2}{2\epsilon\epsilon_0} \quad (2)$$

where ϵ_0 and ϵ are vacuum permittivity and relative permittivity of perovskite, q is elementary charge, and L is thickness of ETL. The V_{TFL} decreased from 0.38 V of pristine SnO_2 to 0.22 V of PAA-EA- SnO_2 , thus the PAA-EA- SnO_2 ETL showed lower trap density of $2.57 \times 10^{17} \text{ cm}^{-3}$ compared to pristine SnO_2 ($4.44 \times 10^{17} \text{ cm}^{-3}$). In the trap-free SCLC region, electron mobility μ_e was obtained using the Mott-Gurney formula

$$J = \frac{9\epsilon\epsilon_0\mu_e V_b^2}{8L^3} \quad (3)$$

where V_b and J are applied voltage and current density. The mobilities μ_e increased from 3.35×10^{-5} for SnO_2 to $8.26 \times 10^{-5} \text{ cm}^2 \text{ V}^{-1} \text{ s}^{-1}$ for PAA-EA- SnO_2 , suggesting improved charge transport in PAA-EA modified SnO_2 ETL.

The energy level diagrams for different ETLs were calculated based on ultraviolet photoelectron spectroscopy (UPS) spectra and UV-Vis absorbance spectra (Fig. 3d and Fig. S13), and the calculated energy levels were summarized in Table S2. The Fermi level of PAA-EA- SnO_2 approached to the conduction band minimum (CBM), suggesting n-doping effect of PAA-EA modification in consistent to the conductivity measurement (Fig. 3e). The CBM of SnO_2 and PAA-EA- SnO_2 were -4.21 and -4.07 eV , respectively. The higher CBM of PAA-EA- SnO_2 can offer better energy-level alignment with perovskite to reduce interface energy barriers and facilitate carrier transport, leading to V_{oc} improvement. Kelvin Probe Force Microscopy (KPFM) was used to measure apparent surface potential of ETLs (Fig. 3f), and the surface potential of PAA-EA- SnO_2 was higher than that of pristine SnO_2 . The increase in surface potential suggested that PAA-EA modification can shift the energy level of SnO_2 upward, making it easier for the electrons to transfer from perovskite to SnO_2 ETL, which can eliminate energy loss at interface and improve overall efficiency of the solar cell.

Surface property of substrate is crucial for morphology and quality of subsequent perovskite film. Therefore, the surface properties of SnO_2 ETLs were investigated by contact angle measure-

ments (Fig. S14). Contact angle on PAA-EA- SnO_2 film was reduced to 20° from 64° on SnO_2 . Better wettability could reduce nucleation energy and induce larger perovskite grains. As shown in Fig. 4(a), perovskite film deposited on PAA-EA- SnO_2 showed uniform morphology and larger grain size, which was consistent with the slightly enhanced UV-Vis absorption (Fig. S15) and a slight increase in current density. Meanwhile, cross-sectional SEM images revealed that perovskite film deposited on PAA-EA- SnO_2 had perpendicular orientation and neat grains across the entire cross-section, while the pristine film showed a random stack of scattered perovskite grains. No cavity was found at the PAA-EA- SnO_2 ETL/perovskite interface, which was beneficial for interface carrier extraction and environmental stability. The crystallization properties of perovskite films were further studied by XRD (Fig. 4c), and the FWHM of perovskite (110) peak at $2\theta = 13.9^\circ$ narrowed from 0.12° to 0.10° for the pristine and PAA-EA-modified films, respectively (Fig. S16). The $-\text{COO}^-$ groups in PAA-EA strongly interact with PbI_2 , resulting in less dense PbI_2 thin film (Fig. S17). The pores in PbI_2 provide path for organic halide solution penetration and room for volume expansion when PbI_2 is converted to perovskite, leading to a more complete conversion of PbI_2 to perovskite, as also shown by the reduced PbI_2 peak in XRD after PAA-EA modification. The PAA-EA- PbI_2 interaction can be further verified by FTIR and XPS. The characteristic FTIR peak of C=O of $-\text{COO}^-$ shifted from 1532 cm^{-1} in PAA-EA to 1541 cm^{-1} in PAA-EA- PbI_2 mixture (Fig. S18). The binding energy

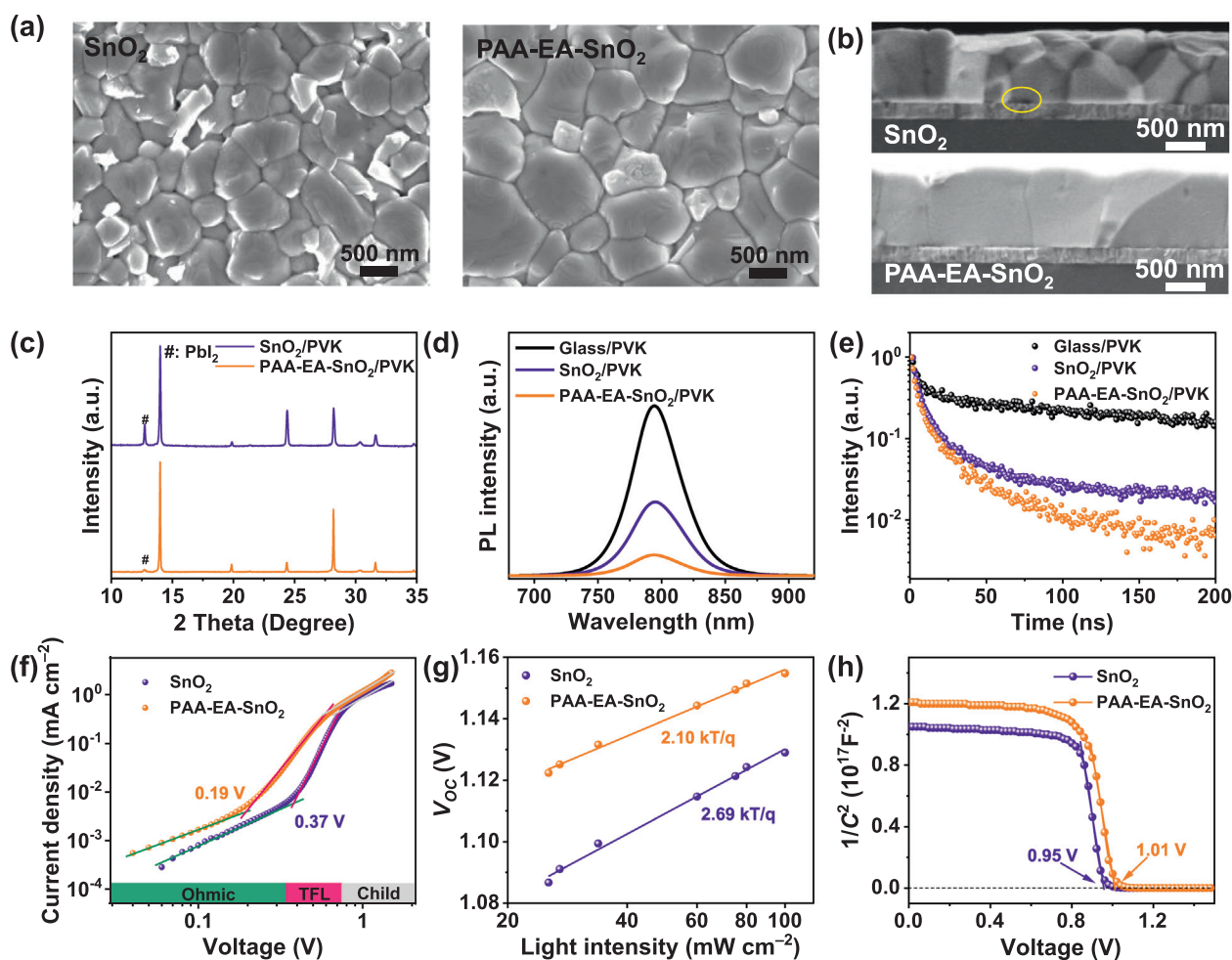


Fig. 4. Morphology and optoelectronic properties. (a, b) The top-view and cross-sectional SEM images of perovskite films deposited on SnO_2 with and without PAA-EA modification. (c) XRD spectra, (d) Steady-state PL and (e) TRPL of perovskite films deposited on SnO_2 and PAA-EA- SnO_2 ETLs. (f) SCLC measurements of pristine and PAA-EA modified devices. (g) Function of V_{oc} and light intensities (Suns- V_{oc}) and (h) Mott-Schottky curves of PSCs with SnO_2 and PAA-EA- SnO_2 ETLs.

of Pb $4f_{7/2}$ and Pb $4f_{5/2}$ peaks for PbI_2 on SnO_2 and PAA-EA- SnO_2 down-shift from 138.5 and 143.4 eV to 138.1 and 143.0 eV (Fig. S19).

Carrier recombination and dynamics behavior in PSCs were studied by steady-state photoluminescence (PL) and time-resolved photoluminescence (TRPL) measurements (Fig. 4d and e). The perovskite film deposited on PAA-EA- SnO_2 showed lower PL intensity compared to the pristine film, indicating higher carrier extraction efficiency of PAA-EA modified ETLs. The average lifetime obtained from TRPL spectra that were fitted by double exponential decay function decreased from 35.9 ns for pristine film to 9.5 ns for PAA-EA-modified film, also suggesting faster electron extraction at ETL and perovskite interface.

To quantify trap density in perovskite film, space charge limited current (SCLC) measurement was adopted, and the dark J - V curves were obtained and shown in Fig. 4(f). The trap-filled limit voltages (V_{TFL}) decreased from 0.37 V of the pristine film to 0.19 V of PAA-EA-modified perovskite film, illustrating the remarkable reduction in trap density from 3.7×10^{15} to $2.9 \times 10^{15} \text{ cm}^{-3}$ by Eq. (2). The Sun- V_{OC} measurement was conducted to illustrate the charge transfer and recombination characteristics of devices (Fig. 4g). The slope decreased from 2.69 kT/q to 2.10 kT/q with modification of PAA-EA, suggesting that trap-assisted recombination was significantly reduced. These results indicated that the $-\text{NH}_3^+$ and $-\text{COO}^-$ groups in the PAA-EA can effectively passivate the halide anionic

defects (FA^+ vacancy) and cationic defects (undercoordinated Pb^{2+}), achieving a lower trap density [57].

Finally, the Mott-Schottky measurement was used to evaluate built-in potential of PSC (Fig. 4h). The built-in potential was found to be higher in the PAA-EA-modified device (1.01 V) than in the pristine device (0.95 V). Higher potential can provide an effective driving force for charge separation and reduce carrier recombination, resulting in a higher V_{OC} . The PAA-EA-modified device also exhibited lower dark current at negative bias than pristine device (Fig. S20), indicating reduced shunting and suppressed charge recombination. Higher dark current at high positive bias of PAA-EA-modified device is consistent with higher conductivity and better electron extraction ability of PAA-EA-modified ETL.

The performance of flexible PSCs was investigated by fabricating device on PET substrates. The champion flexible device with PAA-EA- SnO_2 achieved a PCE of 23.34% with a V_{OC} of 1.162 V, J_{SC} of 24.93 mA cm^{-2} and FF of 80.48%, compared to pristine device of 21.51% (V_{OC} of 1.129 V, J_{SC} of 24.86 mA cm^{-2} and FF of 76.59%) (Fig. 5a). The PAA-EA-modified device achieved a higher stabilized PCE of 23.04% than 20.95% of pristine device as supported by the SPO test (Fig. 5b). IPCE measurement showed a higher integrated J_{SC} of 23.83 mA cm^{-2} for PAA-EA- SnO_2 based flexible PSCs compared to 23.55 mA cm^{-2} for pristine devices (Fig. S21). Large-area (1 cm^2) flexible devices were fabricated and obtained a high PCE up to 21.73% (Fig. 5c).

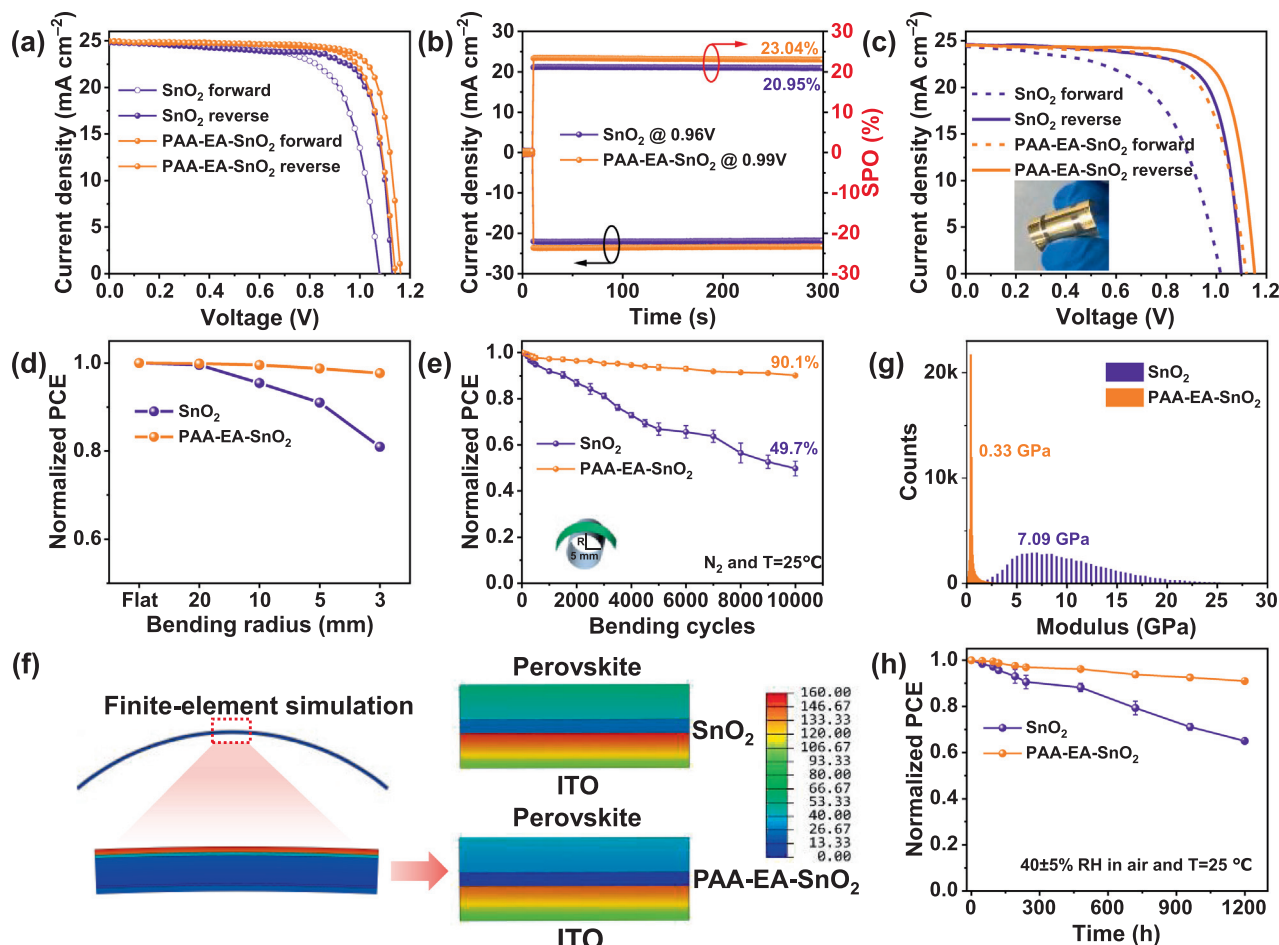


Fig. 5. Performance of flexible device. (a) J - V characteristic curves and (b) SPO of f-PSCs with SnO_2 and PAA-EA- SnO_2 ETLs. (c) J - V characteristic curves of champion PSCs of 1 cm^2 area with different ETLs. (d) Normalized PCE for f-PSCs after bending at different curvature radius for 1000 cycles. (e) Normalized PCE for f-PSCs after 10,000 bending cycles with radius of 5 mm. (f) Stress distribution of flexible devices at bending state near the SnO_2 interface. (g) Young's modulus distribution of SnO_2 and PAA-EA- SnO_2 films. (h) Environmental stability of unencapsulated flexible PSCs.

The flexibility of ETLs was evaluated at various curvature radii ($R = \infty, 20, 10, 5$ and 3 mm) after 1000 bending cycles. The PCE of pristine device dropped sharply to 80% of its initial value when the R decreased to 3 mm, while the PAA-EA-modified device still retained 97% of its initial PCE (Fig. 5d). The device based on PAA-EA-SnO₂ retained 90.1% of its origin PCE after 10,000 bending cycles with a bending radius of 5 mm (Fig. 5e). Conducted cyclic voltammetry was also conducted to characterize the compactness of SnO₂ and PAA-EA-SnO₂ ETLs after bending (Fig. S23). The results indicated that the PAA-EA modification can significantly improve the mechanical durability of the ETLs with lower leakage current after bending. The strong adhesion strength and anchoring of SnO₂ nanoparticles provided by the PAA-EA modification appear to contribute to the improved mechanical robustness of the device as evidenced by the reduced cracking in perovskite films (Fig. S24) and SnO₂ ETLs (Fig. S25) after bending. The quantitative-nanoscale mechanical characterization using AFM peak force revealed that the PAA-EA-SnO₂ film had a lower average Young's Modulus of 0.33 GPa than that of pristine SnO₂ film (7.09 GPa) (Fig. 5g and Fig. S26). The lower Young's Modulus of ETL can effectively reduce the rigidity of the device and ensure better bending resistance. Furthermore, the Young's Modulus of perovskite films deposited on SnO₂ and PAA-EA-SnO₂ were also characterized (Fig. S27), also showing a lower modulus with the modified ETL. Finite element simulation was then used to theoretically analyze overall stress distribution in the bending process, taking into account the Young's Modulus and other mechanical parameters such as Poisson's ratio and film thickness (Table S6). The simulation results showed that PAA-EA-SnO₂ can significantly reduce stress distribution in SnO₂ ETL and PVK films, which was consistent with bending tests and SEM results. Finally, environmental stability of unencapsulated PSCs was measured at 30%–40% relative humidity (Fig. 5h). The PAA-EA modified PSCs retained 92% of the original PCE, while pristine device gradually decreased to 60% after storage for 1000 h. Therefore, the PAA-EA modification can improve both mechanical durability and long-term storage stability of PSCs.

3. Conclusions

In summary, we developed a new water-soluble and adhesive polyelectrolyte binder (PAA-EA) through acid-base neutralization, which was incorporated into SnO₂ colloid to create a hybrid organic–inorganic network. The PAA-EA-SnO₂ showed improved mechanical stability and reduced stress concentration, resulting in enhanced efficiency of flexible PSCs. The champion PCE achieved with PAA-EA-SnO₂ was 24.34% and 23.34% on rigid and flexible substrates, respectively, and showing good reproducibility. Additionally, PAA-EA-SnO₂ exhibited good efficiency of 22.88% in a large-area device (1.00 cm²). The f-PSCs based on PAA-EA-SnO₂ maintained 90.1% of original PCE after 10,000 bending cycles, indicating excellent mechanical stability. These findings demonstrate the potential of using hybrid organic–inorganic composites to develop highly efficient and mechanically stable flexible PSCs, thereby advancing practical application of these devices.

Experimental section

Experimental details can be found in the Supporting Information.

Declaration of competing interest

The authors declare that they have no known competing financial interests or personal relationships that could have appeared to influence the work reported in this paper.

Acknowledgments

This work was supported by the National Key R&D Program of China (2019YFB1503201), the National Natural Science Foundation of China (52172238, 52102304, 51902264), the Natural Science Foundation of Shanxi Province (2020JM-093), the Open project of Shaanxi Laboratory of Aerospace Power (2021SXSYS-01-03), the Science Technology and Innovation Commission of Shenzhen Municipality (JCYJ20190807111605472), and the Fundamental Research Funds for the Central Universities (3102019JC0005, 5000220118).

Appendix A. Supplementary material

Supplementary data to this article can be found online at <https://doi.org/10.1016/j.jechem.2023.06.026>.

References

- [1] S. De Wolf, J. Holovsky, S.J. Moon, P. Loper, B. Niesen, M. Ledinsky, F.J. Haug, J.H. Yum, C. Ballif, *J. Phys. Chem. Lett.* 5 (2014) 1035–1039.
- [2] V. D'Innocenzo, G. Grancini, M.J. Alcocer, A.R. Kandada, S.D. Stranks, M.M. Lee, G. Lanzani, H.J. Snaith, A. Petrozza, *Nat. Commun.* 5 (2014) 3586.
- [3] A. Miyata, P. Mitiglu, O. Plochocka, J.-T.-W. Portugall, S.D. Wang, H.J. Stranks, R.J. Snaith, *Nicholas Nat. Phys.* 11 (2015) 582–587.
- [4] G. Xing, N. Mathews, S. Sun, S.S. Lim, Y.M. Lam, M. Grätzel, S. Mhaisalkar, T.C. Sum, *Science* 342 (2013) 344–347.
- [5] S.D. Stranks, G.E. Eperon, G. Grancini, C. Menelaou, M.J.P. Alcocer, T. Leijtens, L. M. Herz, A. Petrozza, H.J. Snaith, *Science* 342 (2013) 341–344.
- [6] Kojima, K. Teshima, Y. Shirai, T. Miyasaka, *J. Am. Chem. Soc.* 131 (2009) 6050–6051.
- [7] Q. Jiang, Y. Zhao, X. Zhang, X. Yang, Y. Chen, Z. Chu, Q. Ye, X. Li, Z. Yin, J. You. *Nat. Photonics* 13 (2019) 460–466.
- [8] J. Jeong, M. Kim, J. Seo, H. Lu, P. Ahlawat, A. Mishra, Y. Yang, M.A. Hope, F.T. Eickemeyer, M. Kim, Y.J. Yoon, I.W. Choi, B.P. Darwich, S.J. Choi, Y. Jo, J.H. Lee, B. Walker, S.M. Zakeeruddin, L. Emsley, U. Rothlisberger, A. Hagfeldt, D.S. Kim, M. Grätzel, J.Y. Kim, *Nature* 592 (2021) 381–385.
- [9] M.A. Green, E.D. Dunlop, G. Siefer, M. Yoshita, N. Kopidakis, K. Bothe, X. Hao. *Solar Cell Efficiency Tables (version 61)*. 31 (2023) 3–16.
- [10] M. Kim, J. Jeong, H. Lu, T.K. Lee, F.T. Eickemeyer, Y. Liu, I.W. Choi, S.J. Choi, Y. Jo, H.-B. Kim, S.-I. Mo, Y.-K. Kim, H. Lee, N.G. An, S. Cho, W.R. Tress, S.M. Zakeeruddin, A. Hagfeldt, J.Y. Kim, M. Grätzel, D.S. Kim, *Science* 375 (2022) 302–306.
- [11] H. Min, D.Y. Lee, J. Kim, G. Kim, K.S. Lee, J. Kim, M.J. Paik, Y.K. Kim, K.S. Kim, M. G. Kim, T.J. Shin, S. Il Seok, *Nature* 598 (2021) 444–450.
- [12] L. Zhang, C. Fu, S. Wang, M. Wang, R. Wang, S. Xiang, Z. Wang, J. Liu, H. Ma, Y. Wang, Y. Yan, M. Chen, L. Shi, Q. Dong, J. Bian, Y. Shi, *Adv. Funct. Mater.* (2023) 2213961.
- [13] N. Rolston, K.A. Bush, A.D. Printz, A. Gold-Parker, Y. Ding, M.F. Toney, M.D. McGehee, R.H. Dauskardt, *Adv. Energy Mater.* 8 (2018) 1802139.
- [14] H.S. Jung, G.S. Han, N.-G. Park, M.J. Ko, J. Ko, J. Joule 3 (2019) 1850–1880.
- [15] J. Zhang, W. Zhang, H.-M. Cheng, S.R.P. Silva, *Mater. Today* 39 (2020) 66–88.
- [16] Y. Xu, Z. Lin, W. Wei, Y. Hao, S. Liu, J. Ouyang, J. Chang. *Nano Micro Lett.* 14 (2022) 117.
- [17] G. Saianand, P. Sonar, G.J. Wilson, A.-I. Gopalan, V.A.L. Roy, G.E. Unni, K. Mamun Reza, B. Bahrami, K. Venkatramanan, Q. Qiao, J. Energy Chem. 54 (2021) 151–173.
- [18] B. Roose, J.-P.-C. Baena, K.C. Gödel, M. Graetzel, A. Hagfeldt, U. Steiner, A. Abate, *Nano Energy* 30 (2016) 517–522.
- [19] S.S. Shin, E.J. Yeom, W.S. Yang, S. Hur, M.G. Kim, J. Im, J. Seo, J.H. Noh, S.I. Seok, *Science* 356 (2017) 167–171.
- [20] W. Ke, G. Fang, Q. Liu, L. Xiong, P. Qin, H. Tao, J. Wang, H. Lei, B. Li, J. Wan, G. Yang, Y. Yan, *J. Am. Chem. Soc.* 137 (2015) 6730–6733.
- [21] C. Altinkaya, E. Aydin, E. Ugur, F.H. Isikgor, A.S. Subbiah, M. De Bastiani, J. Liu, A. Babayigit, T.G. Allen, F. Laquai, A. Yildiz, S. De Wolf, *Adv. Mater.* 33 (2021) e2005504.
- [22] S.Y. Park, K. Zhu, *Adv. Mater.* 34 (2022) e2110438.
- [23] P. Wu, S. Wang, X. Li, F. Zhang, *J. Mater. Chem. A* 9 (2021) 19554–19588.
- [24] L. Xiong, Y. Guo, J. Wen, H. Liu, G. Yang, P. Qin, G. Fang, *Adv. Funct. Mater.* 28 (2018) 1802757.
- [25] A. Uddin, H. Yi, *Solar RRL* 6 (2022) 2100983.
- [26] Q. Jiang, L. Zhang, H. Wang, X. Yang, J. Meng, H. Liu, Z. Yin, J. Wu, X. Zhang, J. You. *Nat. Energy* 2 (2016) 1543.
- [27] T.A.N. Peiris, H.C. Weerasinghe, M. Sharma, J.-E. Kim, M. Michalska, N. Chandrasekaran, D.C. Senevirathna, H. Li, A.S.R. Chesman, D. Vak, J.J. Jasieniak, *Chem. Mater.* 34 (2022) 5535–5545.
- [28] W.K. Narayanan Lakshminarasimhan, W. Choi, *J. Phys. Chem. C* 112 (2008) 20451–20457.

- [29] T. Bu, J. Li, F. Zheng, W. Chen, X. Wen, Z. Ku, Y. Peng, J. Zhong, Y.B. Cheng, F. Huang, *Nat. Commun.* 9 (2018) 4609.
- [30] G.S. Han, J. Kim, S. Bae, S. Han, Y.J. Kim, O.Y. Gong, P. Lee, M.J. Ko, H.S. Jung, *ACS Energy Lett.* 4 (2019) 1845–1851.
- [31] P. Lv, Y. Yang, N. Li, Y. Zhang, M. Hu, B. Huang, Y. Zhu, Y. Wang, J. Pan, S. Wang, B. Zhang, F. Huang, Y.-B. Cheng, J. Lu, *Chem. Eng. J.* 456 (2023).
- [32] Y. Zhao, F. Ma, F. Gao, Z. Yin, X. Zhang, J. You, *Photonics Res.* 8 (2020) A1.
- [33] M. Saliba, J.-P. Correa-Baena, C.M. Wolff, M. Stollerfoht, N. Phung, S. Albrecht, D. Neher, A. Abate, *Chem. Mater.* 30 (2018) 4193–4201.
- [34] Y. Chen, X. Zuo, Y. He, F. Qian, S. Zuo, Y. Zhang, L. Liang, Z. Chen, K. Zhao, Z. Liu, J. Gou, S.F. Liu, *Adv. Sci.* 8 (2021) 2001466.
- [35] Y. Yang, H. Lu, S. Feng, L. Yang, H. Dong, J. Wang, C. Tian, L. Li, H. Lu, J. Jeong, S. M. Zakeeruddin, Y. Liu, M. Grätzel, A. Hagfeldt, *Energ. Environ. Sci.* 14 (2021) 3447–3454.
- [36] F. Li, C. Gong, B. Fan, Z. Xing, X. Meng, S. Zhang, X. Hu, Y. Chen, *Adv. Funct. Mater.* 32 (2022) 2206412.
- [37] S. Zhang, H. Si, W. Fan, M. Shi, M. Li, C. Xu, Z. Zhang, Q. Liao, A. Sattar, Z. Kang, Y. Zhang, *Angew. Chem. Int. Ed.* 59 (2020) 11573–11582.
- [38] Z. Li, Z. Wang, C. Jia, Z. Wan, C. Zhi, C. Li, M. Zhang, C. Zhang, Z. Li, *Nano Energy* 94 (2022).
- [39] J. Chung, S.S. Shin, K. Hwang, G. Kim, K.W. Kim, D.S. Lee, W. Kim, B.S. Ma, Y.-K. Kim, T.-S. Kim, J. Seo, *Energ. Environ. Sci.* 13 (2020) 4854–4861.
- [40] K.-G. Lim, T.-H. Han, T.-W. Lee, *Energ. Environ. Sci.* 14 (2021) 2009–2035.
- [41] R. Zhao, Z. Gu, P. Li, Y. Zhang, Y. Song, *Adv. Mater. Technol.* 7 (2022) 2101124.
- [42] H. Zhang, N.-G. Park, *Angew. Chem. Int. Ed.* 61 (2022) e202212268.
- [43] H. Liu, Z. Zhang, Z. Su, W. Zuo, Y. Tang, F. Yang, X. Zhang, C. Qin, J. Yang, Z. Li, M. Li, *Adv. Sci.* 9 (2022) 2105739.
- [44] X. Yu, X. Yan, J. Xiao, Z. Ku, J. Zhong, W. Li, F. Huang, Y. Peng, Y.-B. Cheng, J. Chem. Phys. 153 (2020).
- [45] M.A. Rahman, A. Giri, *J. Chem. Phys.* 155 (2021).
- [46] L. Qiu, D. Mei, W.-H. Chen, Y. Yuan, L. Song, L. Chen, B. Bai, P. Du, J. Xiong, *Sol. Energy Mater. Sol. Cells* 248 (2022).
- [47] F. Bella, G. Griffini, J.-P. Correa-Baena, G. Saracco, M. Grätzel, A. Hagfeldt, S. Turri, C. Gerbaldi, *Science* 354 (2016) 203–206.
- [48] C. Liu, M. Guo, H. Su, P. Zhai, K. Xie, Z. Liu, J. Zhang, L. Liu, H. Fu, *Appl. Surf. Sci.* 588 (2022).
- [49] J. Zhang, J. Fu, Q. Chen, H. Ma, Z. Jiang, Z. Zhang, Y. Zhou, B. Song, *Chem. Eng. J.* 433 (2022).
- [50] S. You, H. Zeng, Z. Ku, X. Wang, Z. Wang, Y. Rong, Y. Zhao, X. Zheng, L. Luo, L. Li, S. Zhang, M. Li, X. Gao, X. Li, *Adv. Mater.* 32 (2020) e2003990.
- [51] J. Wei, F. Guo, X. Wang, K. Xu, M. Lei, Y. Liang, Y. Zhao, D. Xu, *Adv. Mater.* 30 (2018) e1805153.
- [52] Z. Dai, S.K. Yadavalli, M. Chen, A. Abbaspourtamijani, Y. Qi, N.P. Padture, *Science* 372 (2021) 618–622.
- [53] W. Huang, L. Zeng, X. Yu, P. Guo, B. Wang, Q. Ma, R.P.H. Chang, J. Yu, M.J. Bedzyk, T.J. Marks, A. Facchetti, *Adv. Funct. Mater.* 26 (2016) 6179–6187.
- [54] Q. Zhao, P. Zhang, M. Antonietti, J. Yuan, *J. Am. Chem. Soc.* 134 (2015) (1855) 11852–11851.
- [55] B. Smitha, S. Sridhar, A.A. Khan, *Macromolecules* 37 (2004) 2233–2239.
- [56] Z. Chen, Q. Cheng, H. Chen, Y. Wu, J. Ding, X. Wu, H. Yang, H. Liu, W. Chen, X. Tang, X. Lu, Y. Li, Y. Li, *Adv. Mater.* 35 (2023) 2300513.
- [57] T. Wang, Y. Li, Q. Cao, J. Yang, B. Yang, X. Pu, Y. Zhang, J. Zhao, Y. Zhang, H. Chen, A. Hagfeldt, X. Li, *Energ. Environ. Sci.* 15 (2022) 4414–4424.